ACS Sustainable Chemistry & Engineering

Research Article

pubs.acs.org/journal/ascecg

# Efficient Separation of Electron–Hole Pairs in Graphene Quantum Dots by $TiO_2$ Heterojunctions for Dye Degradation

Dengyu Pan,*[,†] Jinkai Jiao,[†] Zhen Li,[‡] Yanting Guo,[†] Chuanqi Feng,[†] Yuan Liu,[†] Liang Wang,*[,†] and Minghong Wu[‡]

[†]Institute of Nanochemistry and Nanobiology, Shanghai University, Shanghai 200444, People's Republic of China

[‡]Shanghai Applied Radiation Institute, Shanghai University, Shanghai 200444, People's Republic of China

Supporting Information

**ABSTRACT:** Water-soluble, single-crystalline, and amine-functionalized graphene quantum dots (GQDs) with absorption edge at ~490 nm were synthesized by a molecular fusion method, and stably deposited onto anatase $TiO_2$ nanoparticles under hydrothermal conditions. The effective incorporation of the GQDs extends the light absorption of the $TiO_2$ nanoparticles from UV to a wide visible region. Moreover, amine-functionalized GQD–$TiO_2$ heterojunctions can absorb more $O_2$ than pure $TiO_2$, which can generate more $\cdot O_2$ species for MO degradation. Accordingly, the heterojunctions exhibit much higher photocatalytic performance for degrading methyl orange (MO) under visible-light irradiation than $TiO_2$ alone. At optimum GQD content (1.0 wt %), an apparent MO decomposition rate constant is 15 times higher than that of $TiO_2$ alone, and photocurrent intensity in response to visible-light excitation increases by 9 times. Compared with conventional sensitization by toxic, photounstable quantum dots such as CdSe QDs, the sensitization by environmentally friendly GQDs shows higher visible-light photocatalytic activity and higher cycling stability. Monodispersed QD-based heterojunctions can effectively inhibit the fast recombination of electron–hole pairs of GQDs with a large exciton binding energy. The photogenerated electron transfer, energy-band-matching mechanism of GQD/$TiO_2$, and possible MO decomposition pathways under visible-light irradiation are proposed.

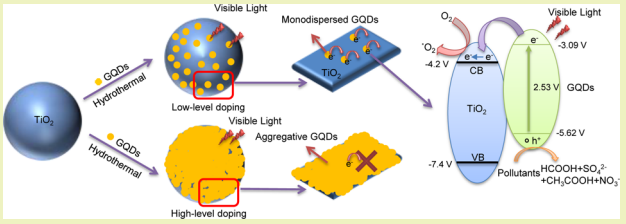


**KEYWORDS:** *Graphene quantum dots, Heterojunctions, Photocatalysis*

## INTRODUCTION

Heterogeneous photocatalysts have drawn great attention in the past decades because of their broad applicability and better performances.[1,2] Among the photocatalysts, anatase titanium dioxide ($TiO_2$) has shown to be promising because of its effectively oxidizing power, good photodurability, environmental friendlies, chemical inertness, and low cost.[3−7] Despite their good performances and stabilities, $TiO_2$-based photocatalysts have limited applications because of a wide bandgap energy (3.2 eV) and high recombination rate. Hence, various research groups have tried to improve their photocatalytic activity using different approaches such as element doping,[6,8−12] sensitization with a visible bandgap semiconductor,[13,14] and use of traditional semiconductor quantum dots (QDs), such as CdX (X = Se, S, Te).[15−17] Among those strategies, typical narrow bandgap QDs of compounds have been reported as the best option spanning the UV as well as the visible portions of the solar spectrum.[15−17] To realize effective separation of photoexcited electrons from holes required for these compounds, it is essential to construct suitable heterojunctions based on QD modified $TiO_2$.[17] Despite the substantial progress, the photocatalytic activity of these photocatalysts is not improved markedly[18] because rich surface traps in naked QDs increase the recombination rate of photoexcited electrons and holes. Moreover, these QDs are known to be highly unstable to hole oxidation in a liquid medium under light irradiation,[19] and the inevitable photo-oxidization seriously impairs these heterojunctions, leading to the photodegradation of their performances. Moreover, there are increasing safety and environmental concerns about these conventional heterojunctions, because highly toxic Cd ions are released into the solution by photo-oxidization.[18,19] Therefore, it is still a challenge to develop high-efficiency, environmentally friendly, and recyclable sensitizers for enhancing solar harvesting capability of heterojunctions under sustainable conditions.

As a novel class of QD materials, graphene quantum dots (GQDs) have currently become an active area of great interest[20−40] because of a myriad of alluring physicochemical properties as well as a wide range of potential applications, such as bioimaging,[26,29,31−33,38] sensors,[34,36] light-emitting devices,[27,28,35] photocatalysis,[20−24,40] and solar cells.[37] Different from toxic and unstable conventional semiconductor QDs, GQDs are environmentally friendly and highly robust against harsh chemical attacks or strong UV-light irradiation. More-

Received: April 21, 2015
Revised: August 26, 2015
Published: August 31, 2015





DOI: 10.1021/acssuschemeng.5b00771
ACS Sustainable Chem. Eng. 2015, 3, 2405−2413

over, GQDs keep the graphene geometry with a high specific surface area and possess stable $sp^2$ bonding at the surface without need of additional passivation to remove surface traps except for edge sites.[20,22,23] Besides, the electronic structure of GQDs is tunable in a wide energy range by changing size and functionalization at edge site,[22,23,28,31,40] which allows for construction of GQD−$TiO_2$ heterojunctions with appropriate energy-band matching while the bandgap of GQDs is tuned as lowly as possible for harvesting more solar light. Despite these conceptual advantages, pure GQDs have a poor catalytic property due to their large exciton binding energy (∼0.8 eV estimated for 2 nm GQDs[41]), which greatly increases the recombination rate of photoexcited electrons and holes. Doping is an effective method to change the electronic density of bulk semiconductor materials and tune their optical, electrical, and transport properties. In the case of bulk graphene, amine-function (or called N-dopant) can induce different effects: amine-functionalized graphene can enhance surface absorption for organic pollutants and $O_2$,[42] which degrade organic matter with a relatively short degradation time. On the basis of the benefits of amine-function in graphene nanostructures, it can be extrapolated that the introduction of amine to GQDs will show similar properties to bulk graphene, which is extremely important both fundamentally and technologically. These surface modifications enable directly exploiting a free graphene surface to construct GQD−$TiO_2$ heterojunctions with fast electron transfer to suppress the electron−hole recombination.[23] Meanwhile, current routes are less effective in mass production of high-quality GQDs. The preparation of GQDs is typically based on chemical or electrochemical cutting methods, and GQDs exhibit defective structure and thus extremely poor optical properties.[20−28,32−40] For example, their absorption bands are largely localized within the UV region, which limits their solar harvesting efficiency for photocatalytic or other applications.

Recently, our group has developed the gram-scale production of single-crystalline and amine-functionalized GQDs based on a water-phase molecular fusion method. The low-cost, mild, and green synthetic method has provided a platform for manipulating their properties and further investigating their potential applications.[31] In the present study, we evaluate the visible-light sensitization capability of single-crystalline and amine-functionalized GQDs with strong visible-light absorption as the environmentally friendly, highly robust sensitizer to sensitize a commercial $TiO_2$ photocatalyst for photodegradation of organic dyes. The most effective junctions of GQDs with $TiO_2$ nanoparticles were established by hydrothermal deposition of the GQDs at a low doping level (1.0 wt %) on the nanoparticles. Importantly, a novel monodispersed QD-based heterojunction can effectively inhibit the fast recombination of excitons of GQDs with a large exciton binding energy. The composite on exposure to visible light exhibits much higher photocatalytic performance for degrading methyl orange (MO) and stronger photocurrent response than $TiO_2$ alone. Moreover, the composite catalyst exhibits excellent long-term photostability with a negligible decrease in degradation rate even after 480 min of irradiation. These results indicate that the GQDs can serve as an effective sensitizer to harvest visible light and the GQD−$TiO_2$ heterojunctions have an ability to suppress the electron−hole recombination and thus enhance the catalytic activity.

## EXPERIMENTAL SECTION

**Chemicals.** All reagents were of analytical grade and used without further purification. Pyrene was obtained from TCI. Water-soluble CdSe QDs with absorption edge at ∼510 nm was supplied by Wuhan Jiayuan Co., Ltd. Tetrabutylammonium hexafluorophosphate ($TBAPF_6$), anatase $TiO_2$ nanoparticles, and poly(3,4-ethylenedioxythiophene)−polystyrenesulfonate (PEDOT−PSS) were purchased from Sigma-Aldrich. Hydrazine hydrate, nitric acid, sulfuric acid, and ammonium hydroxide were obtained from Sinopharm Chemical Reagent CO., Ltd. Deionized (DI) water was produced using a Milli-Q system ($R$ > 18.1 MΩ).

**Preparation of GQDs.** Amine-functionalized GQDs were synthesized through an alkali-catalyzed water-phase molecular fusion method.[31] In a typical procedure, 1 g of pyrene was nitrated into 1,3,6-trinitropyrene in hot $HNO_3$ (80 mL) at 80 °C under refluxing and stirring for 12 h. After cooled to room temperature, the mixture was diluted with DI water (1 L) and filtered through a 0.22 μm microporous membrane to remove the acid. 0.5 g of 1,3,6-trinitropyrene was dispersed in a hydrazine hydrate solution of DI water (40 mL, 0.2 M) by ultrasonication (500 W, 40 kHz) for 2 h. The suspension was transferred to a poly(tetrafluoroethylene) (Teflon)-lined autoclave (100 mL) and heated at 150 °C for 10 h. After cooled to room temperature, the product containing water-soluble GQDs was filtered through a 25 nm microporous membrane to remove traces of insoluble impurities.

**Synthesis of GQD/$TiO_2$ Composites.** The composites were prepared by a hydrothermal deposition method. Typically, $TiO_2$ (0.1 g) was added to 10 mL of GQD solution (0.1 mg $mL^{-1}$) with stirring for 1 h at room temperature to obtain a homogeneous suspension. After that, the suspension was transferred into a poly(tetrafluoroethylene) (Teflon)-lined autoclave (20 mL) and maintained at 150 °C for 4 h, and dried in a vacuum oven at 80 °C overnight. The resulting composite contains 1.0 wt % of GQDs. Other doping contents were controlled by addition of different volumes of the GQD solution. CdSe QD/$TiO_2$ composites were prepared by a similar procedure.

**Photocatalytic Test.** The photodegradation of methyl orange (MO) was carried out by adding 0.02 g of photocatalyst in 50 mL of 10 mg $L^{-1}$ MO solution at room temperature. A 350 W xenon lamp with a cutoff filter ($\lambda$ > 420 nm) was used for visible-light irradiation. Prior to illumination, the suspension was protected from light and magnetically stirred for 1 h to reach adsorption equilibrium, then stirred under visible light all the time. A small amount of suspension (about 1 mL) was taken out every 30 min and filtered through a 0.22 μm microporous membrane. The MO in the suspension was quantified by the measurement of the decay of absorbance at $\lambda_{max}$ = 466 nm at a certain time.

**Electrochemical Measurements.** The cyclic voltammetry (CV) was performed by using a conventional three-electrode system on a CHI 660D electrochemical workstation (Chenhua Instrument, Shanghai, China), which consists of a GQD coated platinum sheet as the working electrode, a platinum wire as the counter electrode, and an Ag/AgCl (saturated KCl) as the reference electrode. CV was recorded in acetonitrile containing 0.1 M $TBAPF_6$ as the supporting electrolyte. The lowest unoccupied molecular orbital (LUMO) energy level of the GQDs was calculated according to the following equation: $E_{LUMO} = -e(E_{red} + 4.4)$ (eV).

**Photocurrent Tests.** Photocurrent measurements were performed in a conventional three-electrode configuration with a Pt foil as the counter electrode and an Ag/AgCl (saturated KCl) reference electrode, and 0.5 M $Na_2SO_4$ as the electrolyte. The working electrodes were prepared as followed: 10 mg of the prepared photocatalyst was ground with 20 μL of a PEDOT−PSS aqueous solution and 100 μL of DI water to make slurry. The slurry was then spread on a 2 cm × 0.5 cm ITO glass substrate with an active area of about 0.5 $cm^2$ by the doctor-blade method. The film was annealed at 150 °C for 30 min in a flowing $N_2$ atmosphere. A 350 W xenon lamp with a cutoff filter ($\lambda$ > 420 nm) was used as light source and placed 3


DOI: 10.1021/acssuschemeng.5b00771
ACS Sustainable Chem. Eng. 2015, 3, 2405−2413

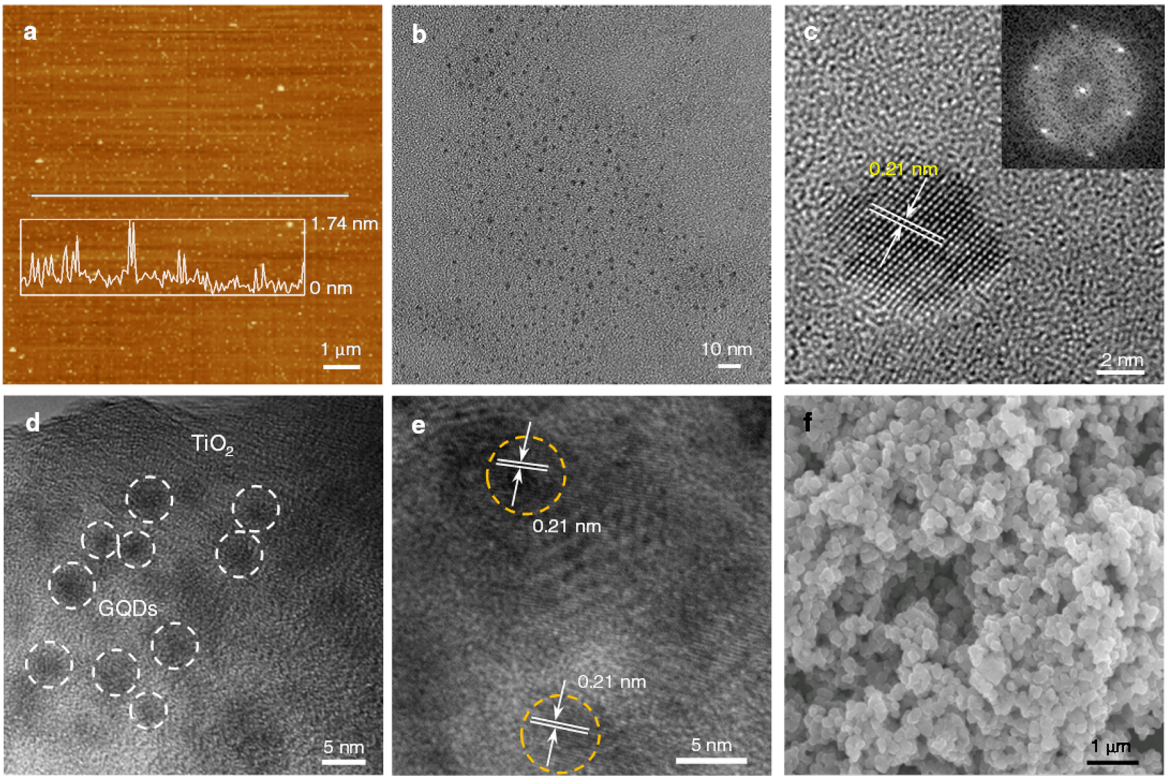


**Figure 1.** AFM image (a), TEM image (b), and HRTEM image (c) of GQDs. TEM (d), HRTEM (e), and SEM (f) images of GQD/$TiO_2$ composite (1.0 wt % doping).

cm away from the working electrode. The photoresponse of the samples as light on and off was measured at 0.0 V.

**Analytical Methods.** Formic acid (HCOOH), acetic acid ($CH_3COOH$), $NO_3^-$, and $SO_4^{2-}$ produced from MO degradation were determined by IC (Dionex ICS1100) equipped with an IonPac As22 column (4 mM × 250 mM). The determination was achieved on hydrophilic anion exchange column. The eluent was mixed with 4.5 mM $Na_2CO_3$ and 1.4 mM $NaHCO_3$ at a flow rate of 1.2 mL $min^{-1}$. The injection volume was 25 $\mu$L.

A triple quadrupole mass spectrometer (HPLC1260-G6460 series, Agilent) operating in negative electrospray ionization (ESI) scan mode was employed for the sample analysis. The LC-MS system was equipped with a C18 reversed-phase column (3.0 mm × 100 mm, 2.7 $\mu$m) with the column temperature at 303 K. Sample injection volume was 10 $\mu$L. The solvent used acetonitrile:0.01 M ammonium acetate (pH 6.8) (30/70, v/v) as the mobile phase with a flow rate of 0.4 mL $min^{-1}$. The ESI conditions were as followed: optimal instrumental source parameters were set as scan time, 200 ms; gas temperature, 300 °C; gas flow, 10 L $min^{-1}$; nebulizer pressure, 40 psi; sheath gas temperature, 350 °C; sheath gas flow, 11 L $min^{-1}$; capillary voltage, −3500 V; nozzle voltage, −1000 V; cell accelerator voltage, 3 V; fragmentor, 100 V. The transitions selected ranged from 100 to 400 $m/z$.

**Structural Characterization.** AFM images were taken using a SPM-9600 atomic force microscope. TEM observations were performed on a JEOL JEM-2010F electron microscope operating at 200 kV. SEM images were taken with JEOL FESEM-6700F under voltage of 15 kV. UV−vis absorption and diffuse reflectance spectra were recorded at room temperature on a Hitachi 3100 spectrophotometer. Raman spectra were recorded on a Renishaw in plus laser Raman spectrometer with $\lambda_{exc}$ = 633 nm. Fourier transform infrared spectroscopy (FT-IR) spectra were performed on Thermo Nicolet Avatar 370 FT-IR. XPS spectra were collected using a Kratos Axis Ultra DLD X-ray photoelectron spectrometer.

## RESULTS AND DISCUSSION

The GQDs were synthesized by an alkali-catalyzed water-phase molecular fusion method.[31] The main process involved 1,3,6-trinitropyrene in an hydrazine hydrate solution of DI water followed by hydrothermal molecular fusion. Brown GQD suspensions were obtained directly by filtering the hydrothermal product with a 25 nm microporous membrane without further dialysis or high-speed centrifugation (Insets in Figure 3a). The size and morphology of the GQDs were examined by AFM, TEM, and HRTEM (Figure 1a,b,c). Their thickness is distributed in the range of 1 to 1.8 nm, with an average thickness of 1.32 ± 0.52 nm (Figure S1, Supporting Information), corresponding to an average layer number of ~3. Their TEM image (Figure 1b) shows that the GQDs have a relatively uniform particle distribution, giving an average lateral size of 3.4 ± 0.6 nm (Figure S2, Supporting Information). As displayed in the HRTEM image (Figure 1c), this real-space image and its fast Fourier transform (FFT) pattern (inset in Figure 1c) show that the GQDs consist of almost defect-free graphene. Moreover, an obvious single-crystal structure is observed, with an interplanar spacing of 0.21 nm corresponding to that of graphene (100) planes. Under the hydrothermal "sintering" conditions, the water-soluble GQDs were deposited stably onto the surface of the $TiO_2$ nanoparticles, without free-standing GQDs in the water. Moreover, the deposited GQDs remain photostable because of their strong $sp^2$ bonding. A typical GQD/$TiO_2$ composite sample with 1.0 wt % doping was characterized by TEM, HRTEM, and SEM. From the typical TEM/SEM images of the composite (Figure 1d,f), it is found that the GQDs are well dispersed on $TiO_2$ nanoparticles with a firm and close contact to form coating-like GQD−$TiO_2$ heterojunctions. EDS element mapping clearly shows the


DOI: 10.1021/acssuschemeng.5b00771
ACS Sustainable Chem. Eng. 2015, 3, 2405−2413

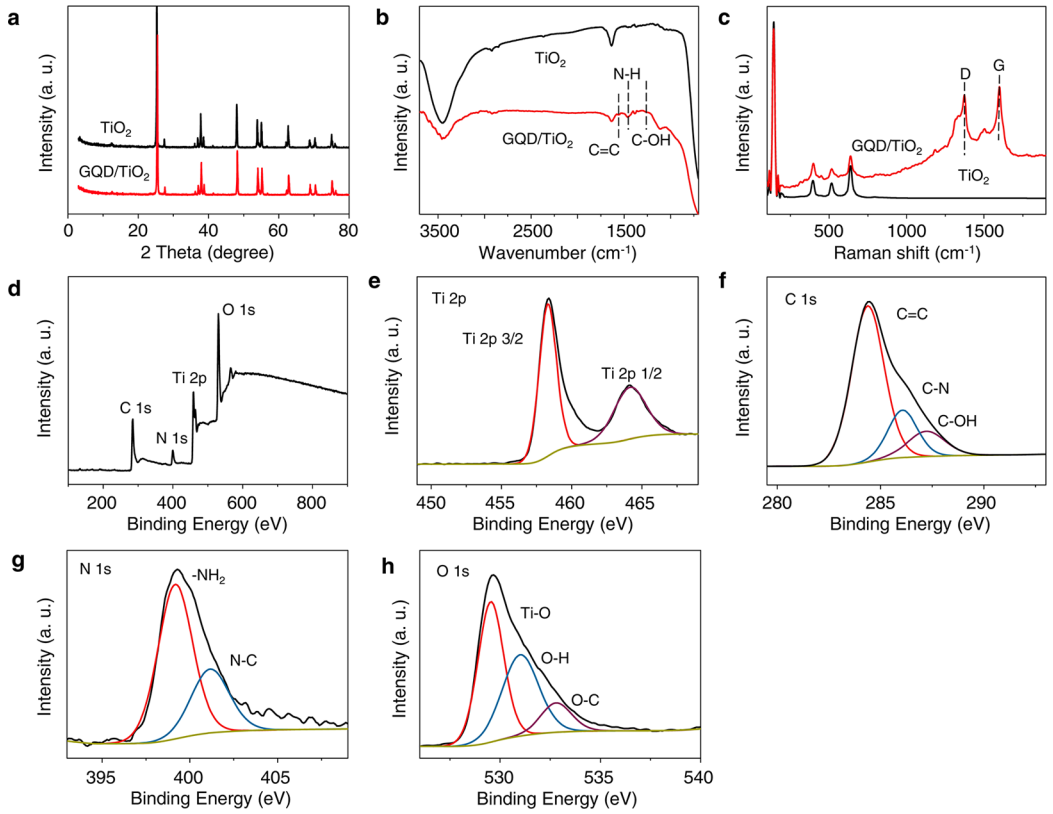


**Figure 2.** XRD (a), FT-IR (b), and Raman (c) spectra of $TiO_2$ alone and 1.0 wt % GQD/$TiO_2$ composite. Survey XPS spectrum (d), high-resolution Ti 2p (e), C 1s (f), N 1s (g), and O 1s (h) spectra of the composite.

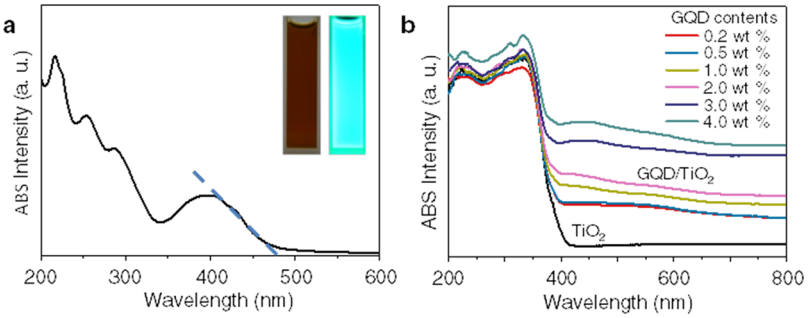


**Figure 3.** (a) UV−vis absorption spectrum of GQD solution. (b) UV−vis absorption spectra of GQD/$TiO_2$ composites with different contents of GQDs. Insets in panel a are the GQD solution under visible (left) and UV (right) lights.

presence of Ti, C, N, and O elements as the major chemical components of the composite over the entire region (Figures S3 and S4, Supporting Information), indicating that the GQDs are evenly distributed on the $TiO_2$ nanoparticles. The presence of the GQDs in the composite is further confirmed by the HRTEM image (Figure 1e), where a 0.21 nm lattice spacing of the graphene (100) planes is identified.

The structure of the composite is further characterized by XRD, FT-IR, Raman, and XPS spectra. As shown in Figure 2a, $TiO_2$ alone and GQD/$TiO_2$ composite exhibit the same diffraction peaks assigned to anatase $TiO_2$ [JCPDS: 21-1272].[43] No characteristic diffraction signals from GQDs are detected in the composite because of the small amount and high dispersion of GQDs in the composite.[44] Compared with the IR spectrum of $TiO_2$, additional IR vibration peaks of the GQDs in the GQD/$TiO_2$ composite are observed (Figure 2b). Besides the C═C vibration at 1590 $cm^{-1}$, there is N—H vibration at 1480 $cm^{-1}$, which is further confirmed by the vibration of C—OH at 1270 $cm^{-1}$ in the IR spectrum. For the Raman spectrum of pure $TiO_2$ (Figure 2c), four strong peaks at 142, 398, 519, and 641 $cm^{-1}$ correspond to the $E_{g(1)}$, $B_{1g(1)}$, $A_{1g}$ + $B_{1g(2)}$, and $Eg_{(3)}$ modes of anatase $TiO_2$, respectively.[13] In the case of the composite, besides the four $TiO_2$ peaks, two additional peaks of the GQDs are observed at 1580 and 1374 $cm^{-1}$, corresponding to the G and D bands of GQDs, respectively. The GQD/$TiO_2$ compositions are also revealed in the XPS spectra (Figure 2d−h). The survey XPS spectrum (Figure 2d) shows strong signals of Ti 2p, C 1s, and O 1s as well as a weak signal from N 1s. This indicates that the GQDs are doped with N. Binding energy peaks at 458.3 and 464.1 eV in the high-resolution Ti 2p spectrum are assigned to Ti $2p_{3/2}$ and Ti $2p_{1/2}$, respectively (Figure 2e). The high-resolution C 1s spectrum (Figure 2f) reveals the strong signal of C═C at 284.2 eV, C—N at 285.4 eV and the distinguishable C—OH peak at 286.9 eV. Two


DOI: 10.1021/acssuschemeng.5b00771
ACS Sustainable Chem. Eng. 2015, 3, 2405−2413

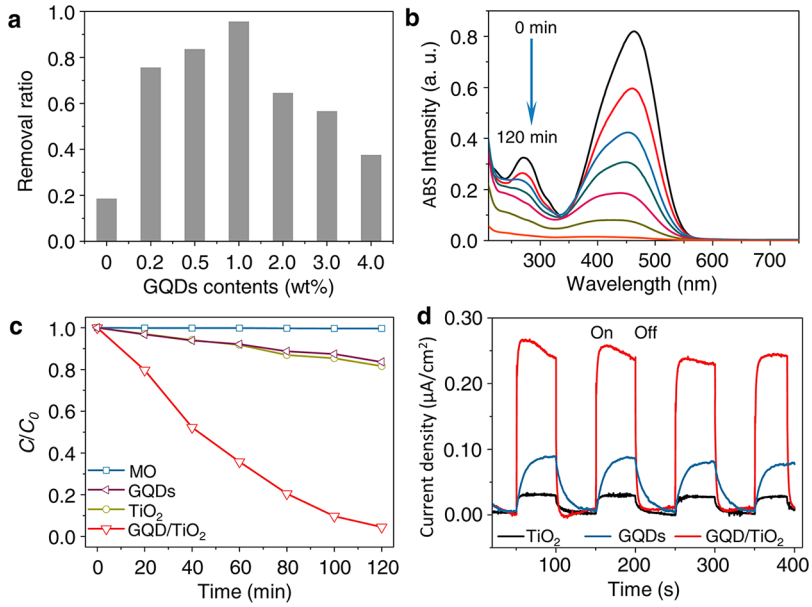


**Figure 4.** (a) Visible-light photocatalytic degradation rates of MO by GQD/$TiO_2$ composites with different contents of GQDs. (b) UV−vis absorption spectra of MO aqueous solution after degraded by visible light in the presence of 1.0 wt % GQD/$TiO_2$ photocatalyst for 0−120 min. (c) Photocatalystic degradation rate curves of MO using GQDs, $TiO_2$, and GQD/$TiO_2$ as photocatalysts under the visible light. (d) Transient photocurrent response spectra of $TiO_2$, GQDs, and GQD/$TiO_2$ composite.

**Scheme 1. (a) Diagrams of Photogenerated Electron Transfer of GQD on the Surface of $TiO_2$ under Visible-Light Irradiation and (b) Diagrams of Energy Position of GQD/$TiO_2$ under Visible-Light Irradiation**

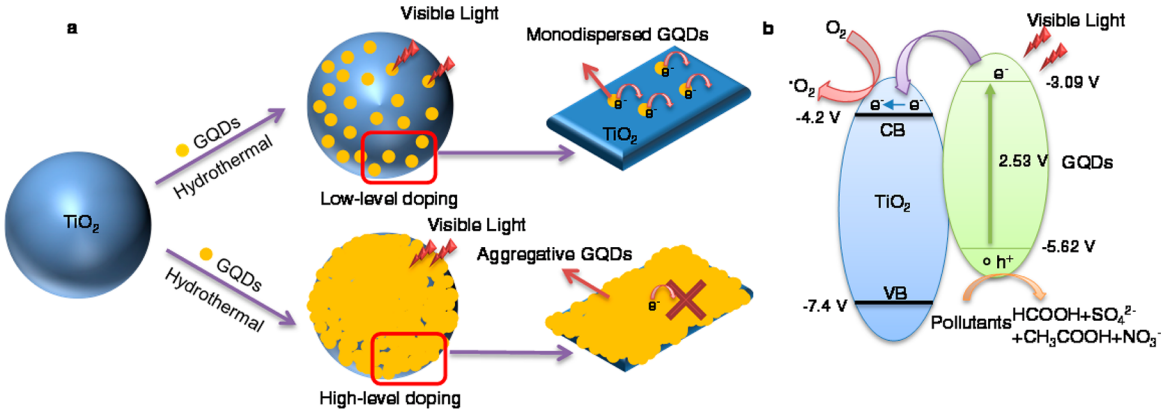


peaks at 399.2 and 401.2 eV in the N 1s XPS spectrum are assigned to $NH_2$ and N—C bonding of the GQDs (Figure 2g). Thus, the primary amine molecules play dual roles in the hydrothermal process: as the precursor for N-dopant and as the passivation agent, which both greatly contribute to the PL enhancement of GQDs.[45] The peaks at 529.2, 531.1, and 533.1 eV in the O 1s spectrum (Figure 2h) are assigned to the Ti—O, O—H, and O—C bonding, respectively. These XPS results are consistent with FT-IR results and further demonstrate the existence of GQDs in the composite.

Figure 3a shows the UV−vis absorption spectrum of as-prepared GQDs. Four pronounced excitonic absorption bands center at about 225, 255, 290, and 405 nm. The absorption edge is at ~490 nm, and thus the optical bandgap of the GQDs is estimated to be 2.53 eV, illustrating that the GQD absorption band extends from UV to visible region (400−500 nm).[46] The insets in Figure 3a depict the GQD solution under visible (left) and UV (right) lights. Obviously, the bright cyan photoluminescence (PL) of GQDs is strong enough to be easily seen with the naked eye, corresponding with the PL spectrum in Figure S5, Supporting Information. As shown in Figure 3b, $TiO_2$ alone exhibits no absorption in the visible region of 400−800 nm. With the incorporation of GQDs, the composites exhibit enhanced visible-light absorption, whose intensity increases with the doping content.[20−24]

To determine an optimum doping content of GQDs for the most efficient MO photocatalytic degradation, we compare the removal ratios of MO using the composite as the photocatalyst with different GQD contents for the same irradiation time of 120 min (Figure 4a). The photodegradation efficiency dramatically rises with slightly increasing the GQD content, rapidly reaches its maximum value merely at 1.0 wt % doping, and then decreases at higher doping levels. At the optimum doping content, the MO dye is nearly completely decoloured after 120 min of visible-light irradiation, as shown by the variations in the UV−vis absorption spectrum and color of MO solution with irradiation time (Figure 4b). The characteristic peaks of MO at 274 and 464 nm rapidly decay upon the


DOI: 10.1021/acssuschemeng.5b00771
ACS Sustainable Chem. Eng. 2015, 3, 2405−2413

**Scheme 2. Proposed Photodegradation Pathway of MO by 1.0 wt %-GQD/$TiO_2$ Photocatalyst under Visible-Light Irradiation**

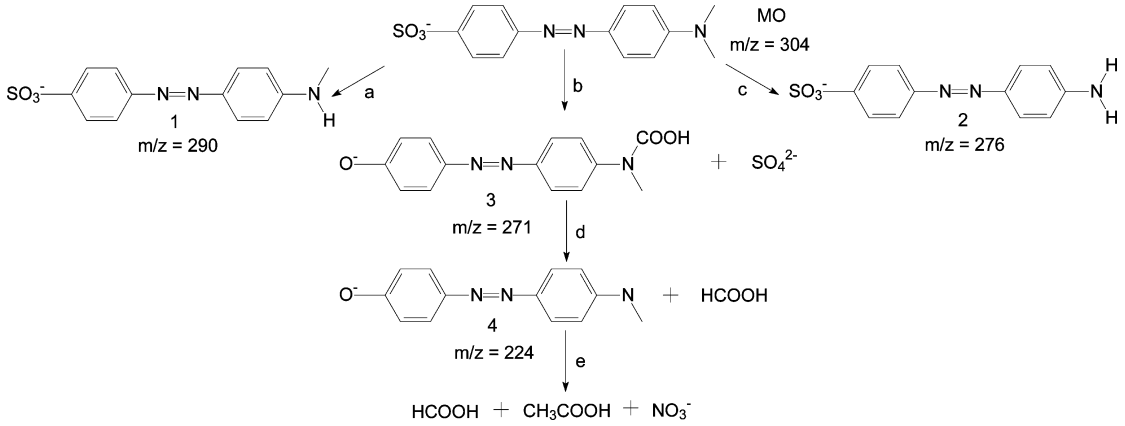


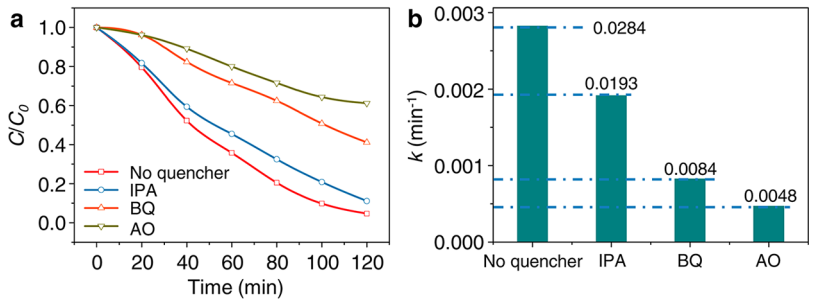


**Figure 5.** Photocatalytic activity (a) and $k_{app}$ values (b) of 1.0 wt %-GQD/$TiO_2$ photocatalyst with different scavenges under visible-light irradiation.

exposure to the visible light and nearly completely disappear after the 120 min treatment. For the pure $TiO_2$ photocatalyst, however, only 18% MO is degraded for the same irradiation time (Figure 4c), as expected by the visible-light response limitation owing to their wide-bandgap nature. GQDs alone also show low catalytic efficiency under the visible light: About 17% MO is degraded after 120 min of irradiation, though they show relatively strong optical absorption in the range of 400–500 nm. The poor catalytic property of pure GQDs can be ascribed to their large exciton binding energy (~0.8 eV estimated for 2 nm GQDs[41]) that greatly increases the recombination rate of photoexcited electrons and holes. These contrast experiments clearly show that the formation of nanoscale heterojunctions between $TiO_2$ nanoparticles and GQDs in the composite plays a key role in the enhanced visible-light catalytic activity. We postulate that a monodispersion and thin monolayer of the soluble GQDs can be deposited on the surface of $TiO_2$ nanoparticles by a hydrothermal process, and thus the optimum GQD–$TiO_2$ heterojunctions at the nanoscale can be established at the low doping level, as shown in Scheme 1a. When the doping content is increased further, a thicker GQD layer forms in the nanoparticle heterojunctions, or GQDs aggregate without direct contact with $TiO_2$ nanoparticles, thus leading to the greatly reduced catalytic activity. For example, at 4.0% doping, the removal ratio of MO is 35%, merely slightly higher than the catalytic capacity of $TiO_2$ nanoparticles alone, though the composite shows stronger visible-light absorption owing to higher GQD doping level. Therefore, for the design of GQD-based hybrid photocatalysts with superior visible-light catalytic performance, it is of crucial importance to construct monodispersed nanoparticle heterojunctions that can effectively inhibit the fast recombination of excitons of GQDs with a large exciton binding energy.

Photoelectrochemical measurements are often used to study qualitatively the excitation and transfer of photogenerated charge carriers in photocatalysts. The transient photocurrent responses of the $TiO_2$, GQDs, and GQD/$TiO_2$ composite are recorded for several on–off cycles under visible-light irradiation and plotted in Figure 4d. For the $TiO_2$ sample, there is weak photocurrent response to visible light, likely because there are oxygen vacancies in the $TiO_2$ nanoparticles, which may induce visible-light response, as reported in many papers.[47] For the GQDs alone, the visible-light on–off response is stronger than in the $TiO_2$ alone, but becomes much slower. There is about 30 s hysteresis to reach the on or off states. This photocurrent hysteresis behavior of the GQDs could be associated with high recombination rate of photoexcited electrons/holes and a high interfacial resistance between $NH_2$-functionalized GQDs to charge transfer. After the hybridization of the GQDs with the $TiO_2$ nanoparticles, the photocurrent response is enhanced by 9 times compared with $TiO_2$ alone, without hysteresis. This result indicates that there exists a good energy-band matching in the GQD–$TiO_2$ heterojunctions, which facilitates highly efficient electron–hole separation at the interface. To confirm this, we measured the CV curve of the GQDs to determine their LUMO. From the reduction potential ($E_{red}$) of −1.31 V vs SCE (Figure S6, Supporting Information), the LUMO energy level relative to the vacuum level is calculated to be −3.09 eV using the equation in the Experimental Section. It is noted that the LUMO of the GQDs locates above the conduction band (CB) bottom (−4.2 eV) of anatase $TiO_2$, giving a large energy difference of 1.11 eV to drive the electron transfer from the CB of the GQDs to the CB of $TiO_2$, as illustrated in Scheme 1b. The electrons were trapped by the adsorbed molecular oxygen


DOI: 10.1021/acssuschemeng.5b00771
ACS Sustainable Chem. Eng. 2015, 3, 2405–2413

on the $TiO_2$ surface to produce superoxide anion ($\cdot O_2^-$) radicals.[48] Electrons left on $TiO_2$ also could be trapped to form $\cdot O_2^-$ radicals. The enhanced transient photocurrent response in the composite can be thus explained based on the frame of GQD−$TiO_2$ heterojunctions, where GQDs are excited by photons of visible light to produce electron−hole couples with a large binding energy (<1 eV), followed by rapid separation and transfer of the charge carriers driven by the large CB difference, thus producing photocurrent transport in the $TiO_2$ matrix.

Similar photophysical processes coupled with photochemical processes occur in the heterojunctions and their interface with MO solution, when the MO molecules are degraded by photocatalysis (Scheme 2). Accompanying the photophysical processes above-mentioned, typical photochemical processes include the production of highly oxidative species such as $h^+$, $\cdot O_2^-$, and ·OH, which have been suggested to directly oxide dye molecules.[1,49,50] To determine the contributions of these reactive species to the MO degradation, we performed MO photocatalytic degradation experiments in the presence of scavengers to quench $h^+$, $\cdot O^{2-}$, and ·OH during the degradation of MO using ammonium oxalate (AO), benzoquinone (BQ), and isopropyl alcohol (IPA), respectively.[1,49,50] Compared with the absence of any scavengers, the addition of all the three scavengers suppresses the MO decomposition rate (Figure 5a), indicating that all the oxidative species contribute to the MO degradation. The contributions of $h^+$, $\cdot O^{2-}$, and ·OH to the overall MO degradation rate are thus determined to be 44.7%, 38.0%, and 17.3%, respectively. These results indicate that $h^+$ and $\cdot O^{2-}$ are the main oxidative species for the MO degradation. The largest contribution of $h^+$ to the degradation is expected because other reactive species are generated after $h^+$. We note that the production of the $\cdot O^{2-}$ species undergoes two basic processes, i.e., electron transfer from the CB of the GQDs to the CB of $TiO_2$ followed by trapping by $O_2$ absorbed on the surface of $TiO_2$ nanoparticles. Moreover, $NH_2$-functionalized GQDs can enhance surface absorption for $O_2$,[41] which were absorbed more $O_2$ on the surface of GQD−$TiO_2$ heterojunctions than pure $TiO_2$. Despite the multistep formation, the $\cdot O^{2-}$ species contributes 38.0%. This fact indicates that the electron transfer process is highly effective owing to the presence of the ideal heterojunctions. Because this species forms on the surface of $TiO_2$ nanoparticles, the $NH_2$-functionalized GQDs should be sparsely dispersed on the surface of $TiO_2$ nanoparticles. Therefore, to enhance the contribution of $\cdot O^{2-}$ species, the doping of the GQDs should be controlled at rather low level, such as the optimum content of 1.0 wt %.

To investigate the degradation mechanism, the degradation products of MO were analyzed by IC and HPLC-MS/MS. Simple inorganic anions of $NO_3^-$ and $SO_4^{2-}$ and small organic acids of formic acid (HCOOH) and acetic acid ($CH_3COOH$) as final products[50−52] were detected by IC (Figure 6). With increasing irradiation time, the concentrations of HCOOH and $SO_4^{2-}$ always increase, but the concentrations of $CH_3COOH$ and $NO_3^-$ remain low during 120 min irradiation. Typical intermediates generated in the degradation of MO after 60 min irradiation can be identified by HPLC-MS/MS (Figure S7, Supporting Information). The mass peak at $m/z$ 304.0 is ascribed to pristine MO molecules, and peaks at $m/z$ 306, 290, 276, 271, and 224 belong to side-chain oxidation products, which have been identified by Fu[53,54] and Peng[55] et al. According to the analysis of IC and HPLC-MS/MS, we have

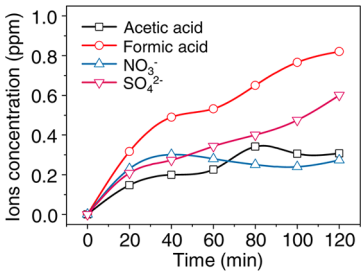


**Figure 6.** IC analysis of degradation products of MO by 1.0 wt %-GQD/$TiO_2$ photocatalyst under visible-light irradiation.

inferred possible reaction pathways during the photocatalytic MO degradation (Scheme 2).

Finally, the cycling stability of the composite is evaluated for four cycles (120 min irradiation at every cycle). For comparison, a composite of water-soluble CdSe QDs and $TiO_2$ nanoparticles was also tested. For the GQD-based composite, the degradation rate of MO is kept at 96% for the four cycles, indicating that the composite is highly photostable. For the CdSe QD/$TiO_2$ photocatalyst, the MO degradation rate decreases from 60% for the first cycle to 48% for the fourth cycle (Figure 7). This photoinduced serious instability is due to

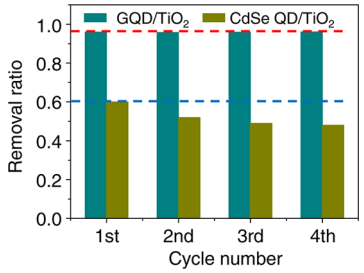


**Figure 7.** Cycling stability experiments of MO by GQD/$TiO_2$ and CdSe QD/$TiO_2$ composites.

the known photo-oxidation reaction $CdX(s) + 2h^+ = Cd^{2+}(l) + X(s)$, which also produces highly toxic $Cd^{2+}$ ions.[18,19] These results indicate that graphene-based QDs are superior to conventional QDs in catalytic activity, recycling usage, and environmental friendliness.

## CONCLUSIONS

In summary, water-soluble and amine-functionalized GQDs are successfully loaded onto the $TiO_2$ in optimum density to form novel GQD sensitized $TiO_2$ heterojunctions. The incorporation of GQDs can sensitize $TiO_2$ and extend the photoresponse of the composite to the visible region. More importantly, amine-functionalized GQD−$TiO_2$ heterojunctions can absorb more $O_2$ on their surface than pure $TiO_2$, which can generate more $\cdot O^{2-}$ species for MO degradation. Compared with pure GQDs and $TiO_2$, the GQD/$TiO_2$ composite exhibits much higher visible-light-driven photocatalytic performance for degrading MO in water. The optimum visible performance is achieved at GQD content of 1 wt %, with an apparent decomposition rate constant 15 times higher than that of pure $TiO_2$, and photocurrent intensity in response to visible-light excitation increases by 9 times. The cycling stability of the composite is better than that of the CdSe QD/$TiO_2$ composite. The enhanced photocatalytic activity can be attributed to the efficient separation and recombination preventing of electron−


DOI: 10.1021/acssuschemeng.5b00771
ACS Sustainable Chem. Eng. 2015, 3, 2405−2413

hole pairs based on a novel monodispersed QD-based heterojunctions. The possible pathway of the photocatalytic decomposition of MO has been proposed. The GQD sensitized photocatalyst is a promising photocatalytic material that has good potential for application to pollutant purification.

## ■ ASSOCIATED CONTENT

### Supporting Information

The Supporting Information is available free of charge on the ACS Publications website at DOI: 10.1021/acssuschemeng.5b00771.

Height distribution of AFM image, lateral size distribution of TEM image, PL and PLE spectrum, and CV curve of GQDs, EDS spectrum and EDS element mapping dates of 1 wt %-GQD/$TiO_2$ composites, and HPLC-MS/MS spectrum of the aqueous MO solution after 60 min photocatalytic treatment over 1 wt %-GQD/$TiO_2$ composite (PDF).

## ■ AUTHOR INFORMATION


### Corresponding Authors

*D. Pan. E-mail: dypan617@shu.edu.cn.

*L. Wang. E-mail: wang198465@163.com.


### Notes

The authors declare no competing financial interest.

## ■ ACKNOWLEDGMENTS

This work has been supported by National Natural Science Foundation of China (No. 11174194, 91233102), the Innovation Program of Shanghai Municipal Education Commission (No. 13YZ017), Program for Changjiang Scholars and Innovative Research Team in University (No. IRT13078), China Postdoctoral Science Foundation funded project (2012M520874), and Shanghai Postdoctoral Scientific Program (13R21413100).

## ■ REFERENCES


(1) Pawar, R. C.; Lee, C. S. Single-step sensitization of reduced graphene oxide sheets and CdS nanoparticles on ZnO nanorods as visible-light photocatalysts. *Appl. Catal., B* **2014**, *144*, 57−65.

(2) Ida, S.; Kim, N.; Ertekin, E.; Takenaka, S.; Ishihara, T. Photocatalytic reaction centers in two-dimensional titanium oxide crystals. *J. Am. Chem. Soc.* **2015**, *137*, 239−244.

(3) Li, S. X.; Chen, J.; Zheng, F. Y.; Li, Y. C.; Huang, F. Y. Synthesis of the double-shell anatase-rutile $TiO_2$ hollow spheres with enhanced photocatalytic activity. *Nanoscale* **2013**, *5*, 12150−12155.

(4) Pu, Y. C.; Wang, G. M.; Chang, K. D.; Ling, Y. C.; Lin, Y. K.; Fitzmorris, B. C.; Liu, C. M.; Lu, X. H.; Tong, Y. X.; Zhang, J. Z.; Hsu, Y. J.; Li, Y. Au nanostructure-decorated $TiO_2$ nanowires exhibiting photoactivity across entire UV-visible region for photoelectrochemical water splitting. *Nano Lett.* **2013**, *13*, 3817−3823.

(5) Chen, X. B.; Liu, L.; Yu, P. Y.; Mao, S. S. Increasing solar absorption for photocatalysis with black hydrogenated titanium dioxide nanocrystals. *Science* **2011**, *331*, 746−750.

(6) Asahi, R.; Morikawa, T.; Ohwaki, T.; Aoki, K.; Taga, Y. Visible-light photocatalysis in nitrogen-doped titanium oxides. *Science* **2001**, *293*, 269−271.

(7) Zhang, Y. Q.; Ma, D. K.; Zhang, Y. G.; Chen, W.; Huang, S. M. N-doped carbon quantum dots for $TiO_2$-based photocatalysts and dye-sensitized solar cells. *Nano Energy* **2013**, *2*, 545−552.

(8) Wang, S.; Pan, L.; Song, J. J.; Mi, W.; Zou, J. J.; Wang, L.; Zhang, X. Titanium-defected undoped anatase $TiO_2$ with p-type conductivity, room-temperature ferromagnetism, and remarkable photocatalytic performance. *J. Am. Chem. Soc.* **2015**, *137*, 2975−2983.

(9) Fei, J.; Li, J. Controlled preparation of porous $TiO_2$-Ag nanostructures through supramolecular assembly for plasmon-enhanced photocatalysis. *Adv. Mater.* **2015**, *27*, 314−319.

(10) Yu, X.; Liu, J.; Yu, Y.; Zuo, S.; Li, B. Preparation and visible light photocatalytic activity of carbon quantum dots/$TiO_2$ nanosheet composites. *Carbon* **2014**, *68*, 718−724.

(11) Wang, J.; Gao, M.; Ho, G. W. Bidentate-complex-derived $TiO_2$/carbon dot photocatalysts: *in situ* synthesis, versatile heterostructures, and enhanced $H_2$ evolution. *J. Mater. Chem. A* **2014**, *2*, 5703−5709.

(12) Yu, H.; Zhao, Y.; Zhou, C.; Shang, L.; Peng, Y.; Cao, Y.; Wu, L. Z.; Tung, C. H.; Zhang, T. carbon quantum dots/$TiO_2$ composites for efficient photocatalytic hydrogen evolution. *J. Mater. Chem. A* **2014**, *2*, 3344−3351.

(13) Youngblood, W. J.; Lee, S. H. A.; Maeda, K.; Mallouk, T. E. Visible light water splitting using dye-sensitized oxide semiconductors. *Acc. Chem. Res.* **2009**, *42*, 1966−1973.

(14) Liu, L. C.; Gu, X. R.; Sun, C. Z.; Li, H.; Deng, Y.; Gao, F.; Dong, L. *In situ* loading of ultra-small $Cu_2O$ particles on $TiO_2$ nanosheets to enhance the visible-light photoactivity. *Nanoscale* **2012**, *4*, 6351−6359.

(15) Zhou, H.; Pan, J.; Ding, L.; Tang, Y.; Ding, J.; Guo, Q.; Fan, T.; Zhang, D. Biomass-derived hierarchical porous CdS/M/$TiO_2$ (M = Au, Ag, pt, pd) ternary heterojunctions for photocatalytic hydrogen evolution. *Int. J. Hydrogen Energy* **2014**, *39*, 16293−16301.

(16) Wang, P.; Li, D.; Chen, J.; Zhang, X.; Xian, J.; Yang, X.; Zheng, X.; Li, X.; Shao, Y. A novel and green method to synthesize CdSe quantum dots-modified $TiO_2$ and its enhanced visible light photocatalytic activity. *Appl. Catal., B* **2014**, *160*, 217−226.

(17) Li, J.; Cushing, S. K.; Zheng, P.; Senty, T.; Meng, F.; Bristow, A. D.; Manivannan, A.; Wu, N. Solar hydrogen generation by a CdS-Au-$TiO_2$ sandwich nanorod array enhanced with Au nanoparticle as electron relay and plasmonic photosensitizer. *J. Am. Chem. Soc.* **2014**, *136*, 8438−8449.

(18) Hodes, G. J. Comparison of dye- and semiconductor-sensitized porous nanocrystalline liquid junction solar cells. *J. Phys. Chem. C* **2008**, *112*, 17778−17787.

(19) Lee, Y. L.; Chang, C. H. Efficient polysulfide electrolyte for CdS quantum dot-sensitized solar cells. *J. Power Sources* **2008**, *185*, 584−588.

(20) Ryu, J.; Lee, E.; Lee, S.; Jang, J. Fabrication of graphene quantum dot-decorated graphene sheets via chemical surface modification. *Chem. Commun.* **2014**, *50*, 15616−15618.

(21) Gupta, B. K.; Kedawat, G.; Agrawal, Y.; Kumar, P.; Dwivedi, J.; Dhawan, S. K. A novel strategy to enhance ultraviolet light driven photocatalysis from graphene quantum dots infilled $TiO_2$ Nanotube Arrays. *RSC Adv.* **2015**, *5*, 10623−10631.

(22) Feng, L.; Tang, X. Y.; Zhong, Y. X.; Liu, Y. W.; Song, X. H.; Deng, S. L.; Xie, S. Y.; Yan, J. W.; Zheng, L. S. Ultra-bright alkylated graphene quantum dots. *Nanoscale* **2014**, *6*, 12635−12643.

(23) Qu, D.; Zheng, M.; Du, P.; Zhou, Y.; Zhang, L.; Li, D.; Tan, H.; Zhao, Z.; Xie, Z.; Sun, Z. Highly luminescent S, N co-doped graphene quantum dots with broad visible absorption bands for visible light photocatalysts. *Nanoscale* **2013**, *5*, 12272−12277.

(24) Pan, D.; Xi, C.; Li, Z.; Wang, L.; Chen, Z.; Lu, B.; Wu, M. Electrophoretic fabrication of highly robust, efficient, and benign heterojunction photoelectrocatalysts based on graphene-quantum-dot sensitized $TiO_2$ nanotube arrays. *J. Mater. Chem. A* **2013**, *1*, 3551−3555.

(25) Pan, D.; Zhang, J.; Li, Z.; Wu, M. Hydrothermal route for cutting graphene sheets into blue-luminescent graphene quantum dots. *Adv. Mater.* **2010**, *22*, 734−737.

(26) Xue, Q.; Huang, H.; Wang, L.; Chen, Z.; Wu, M.; Li, Z.; Pan, D. Nearly monodisperse graphene quantum dots fabricated by amine-assisted cutting and ultrafiltration. *Nanoscale* **2013**, *5*, 12098−12103.

(27) Li, Y.; Hu, Y.; Zhao, Y.; Shi, G.; Deng, L.; Hou, Y.; Qu, L. An electrochemical avenue to green-luminescent graphene quantum dots as potential electron-acceptors for photovoltaics. *Adv. Mater.* **2011**, *23*, 776−780.

(28) Tang, L.; Ji, R.; Li, X.; Bai, G.; Liu, C. P.; Hao, J.; Lin, J.; Jiang, H.; Teng, K. S.; Yang, Z.; Lau, S. P. Deep ultraviolet to near-infrared

emission and photoresponse in layered N-doped graphene quantum dots. *ACS Nano* **2014**, *8*, 6312−6320.
(29) Ge, J.; Lan, M.; Zhou, B.; Liu, W.; Guo, L.; Wang, H.; Jia, Q.; Niu, G.; Huang, X.; Zhou, H.; Meng, X.; Wang, P.; Lee, C. S.; Zhang, W.; Han, X. A graphene quantum dot photodynamic therapy agent with high singlet oxygen generation. *Nat. Commun.* **2014**, *5*, 4596−4604.
(30) Ye, R.; Xiang, C.; Lin, J.; Peng, Z.; Huang, K.; Yan, Z.; Cook, N. P.; Samuel, E. L. G.; Hwang, C. C.; Ruan, G.; Ceriotti, G.; Raji, A. R. O.; Marti, A. A.; Tour, J. M. Coal as an abundant source of graphene quantum dots. *Nat. Commun.* **2013**, *4*, 2943−2949.
(31) Wang, L.; Wang, Y.; Xu, T.; Liao, H.; Yao, C.; Liu, Y.; Li, Z.; Chen, Z.; Pan, D.; Sun, L.; Wu, M. Gram-scale synthesis of single-crystalline grapheme quantum dots with superior optical properties. *Nat. Commun.* **2014**, *5*, 5357−5366.
(32) Nurunnabi, M.; Khatun, Z.; Huh, K. M.; Park, S. Y.; Lee, D. Y.; Cho, K. J.; Lee, Y. K. *In vivo* biodistribution and toxicology of carboxylated graphene quantum dots. *ACS Nano* **2013**, *7*, 6858−6867.
(33) Chong, Y.; Ma, Y.; Shen, H.; Tu, X.; Zhou, X.; Xu, J.; Dai, J.; Fan, S.; Zhang, Z. The *in vitro* and *in vivo* toxicity of graphene quantum dots. *Biomaterials* **2014**, *35*, 5041−5048.
(34) Shen, P.; Xia, Y. Synthesis-modification integration: one-step fabrication of boronic acid functionalized carbon dots for fluorescent blood sugar sensing. *Anal. Chem.* **2014**, *86*, 5323−5329.
(35) Kwon, W.; Kim, Y. H.; Lee, C. L.; Lee, M.; Choi, H. C.; Lee, T. W.; Rhee, S. W. Electroluminescence from graphene quantum dots prepared by amidative cutting of tattered graphite. *Nano Lett.* **2014**, *14*, 1306−1311.
(36) Zhu, H. H.; Liu, A.; Xu, Y. H.; Shan, F. K.; Li, A. H.; Wang, J. M.; Yang, W. R.; Barrow, C.; Liu, J. Q. Graphene quantum dots directly generated from graphite via magnetron sputtering and the application in thin-film transistors. *Carbon* **2015**, *88*, 225−232.
(37) Wang, Z. F.; Zeng, H.; Sun, L. Graphene quantum dots: versatile photoluminescence for energy, biomedical, and environmental applications. *J. Mater. Chem. C* **2015**, *3*, 1157−1165.
(38) Yuan, F.; Ding, L.; Li, Y.; Li, X.; Fan, L.; Zhou, S.; Fang, D.; Yang, S. Multicolor fluorescent graphene quantum dots colorimetrically responsive to all-pH and a wide temperature range. *Nanoscale* **2015**, *7*, 11727−11733.
(39) Liu, Y. S.; Gao, B.; Qiao, Z. Q.; Hu, Y. J.; Zheng, W. F.; Zhang, L.; Zhou, Y.; Ji, G. B.; Yang, G. Gram-scale synthesis of graphene quantum dots from single carbon atoms growth via energetic material deflagration. *Chem. Mater.* **2015**, *27*, 4319−4327.
(40) Yeh, T. F.; Chen, S. J.; Teng, H. S. Synergistic effect of oxygen and nitrogen functionalities for graphene-based quantum dots used in photocatalytic $H_2$ production from water decomposition. *Nano Energy* **2015**, *12*, 476−485.
(41) Li, L. S.; Yan, X. Colloidal graphene quantum dots. *J. Phys. Chem. Lett.* **2010**, *1*, 2572−2576.
(42) Gong, K. P.; Du, F.; Xia, Z. H.; Durstock, M.; Dai, L. M. Nitrogen-doped carbon nanotube arrays with high electrocatalytic activity for oxygen reduction. *Science* **2009**, *323*, 760−764.
(43) Li, N.; Liu, G.; Zhen, C.; Li, F.; Zhang, L.; Cheng, H. M. Battery performance and photocatalytic activity of mesoporous anatase $TiO_2$ nanospheres/graphene composites by template-free self-assembly. *Adv. Funct. Mater.* **2011**, *21*, 1717−1722.
(44) Tian, J.; Leng, Y. H.; Zhao, Z. H.; Xia, Y.; Sang, Y. H.; Hao, P.; Zhan, J.; Li, M. C.; Liu, H. Carbon quantum dots/hydrogenated $TiO_2$ nanobelt heterostructures and their broad spectrum photocatalytic properties under UV, visible, and near-infrared irradiation. *Nano Energy* **2015**, *11*, 419−427.
(45) Liu, S.; Tian, J. Q.; Wang, L.; Zhang, Y. W.; Qin, X. Y.; Luo, Y. L.; Asiri, A. M.; Al-Youbi, A. O.; Sun, X. P. Hydrothermal treatment of grass: a low-cost, green route to nitrogen-doped, carbon-rich, photoluminescent polymer nanodots as an effective fluorescent sensing platform for label-free detection of Cu(II) ions. *Adv. Mater.* **2012**, *24*, 2037−2041.
(46) Wu, H. B.; Hng, H. H.; Lou, X. W. Direct synthesis of anatase $TiO_2$ nanowires with enhanced photocatalytic activity. *Adv. Mater.* **2012**, *24*, 2567−2571.
(47) Ren, F. Z.; Li, H. Y.; Wang, Y. X.; Yang, J. J. Enhanced photocatalytic oxidation of propylene over V-doped $TiO_2$ photocatalyst: Reaction mechanism between $V^{5+}$ and single-electron-trapped oxygen vacancy. *Appl. Catal., B* **2015**, *176*, 160−172.
(48) Fujishima, A.; Rao, T. N.; Tryk, D. A. Titanium dioxide photocatalysis. *J. Photochem. Photobiol., C* **2000**, *1*, 1−21.
(49) Zhao, W.; Liang, F.; Jin, Z. M.; Shi, X. B.; Yin, P. H.; Wang, X. R.; Sun, C.; Gao, Z. Q.; Liao, L. S. Efficient plasmonic photocatalytic activity on silver-nanoparticle-decorated $AgVO_3$ nanoribbons. *J. Mater. Chem. A* **2014**, *2*, 13226−13231.
(50) Okte, A. N.; Yilmaz, O. Photodecolorization of methyl orange by yttrium incorporated $TiO_2$ supported ZSM-5. *Appl. Catal., B* **2008**, *85*, 92−102.
(51) Okte, A. N.; Yilmaz, O. Characteristics of lanthanum loaded $TiO_2$-ZSM-5 photocatalysts: Decolorization and degradation processes of methyl orange. *Appl. Catal., A* **2009**, *354*, 132−142.
(52) Xu, S. B.; Zhu, Y. F.; Jiang, L.; Dan, Y. Visible light induced photocatalytic degradation of methyl orange by polythiophene/$TiO_2$ composite particles. *Water, Air, Soil Pollut.* **2010**, *213*, 151−159.
(53) Li, W. J.; Li, D. Z.; Xian, J. J.; Chen, W.; Hu, Y.; Shao, Y.; Fu, X. Z. Specific analyses of the active species on $Zn_{0.28}Cd_{0.72}S$ and $TiO_2$ photocatalysts in the degradation of methyl orange. *J. Phys. Chem. C* **2010**, *114*, 21482−21492.
(54) Sun, M.; Li, D. Z.; Li, W. J.; Chen, Y. B.; Chen, Z. X.; He, Y. H.; Fu, X. Z. New photocatalyst, $Sb_2S_3$, for degradation of methyl orange under visible-light irradiation. *J. Phys. Chem. C* **2008**, *112*, 18076−18081.
(55) Dai, K.; Chen, H.; Peng, T. Y.; Ke, D. N.; Yi, H. B. Photocatalytic degradation of methyl orange in aqueous suspension of mesoporous titania nanoparticles. *Chemosphere* **2007**, *69*, 1361−1367.


DOI: 10.1021/acssuschemeng.5b00771
*ACS Sustainable Chem. Eng.* 2015, 3, 2405−2413